Chapter 3

Compressive Reflector Antenna Phased Array

Ali Molaei, Juan Heredia Juesas and

Jose Angel Martinez Lorenzo

Additional information is available at the end of the chapter

http://dx.doi.org/10.5772/67663

Abstract

Conventional phased array imaging systems seek to reconstruct a target in the imaging domain by employing many transmitting and receiving antenna elements. These systems are suboptimal, due to the often large mutual information existing between two successive measurements. This chapter describes a new phased array system, which is based on the use of a novel compressive reflector antenna (CRA), that is capable of providing high sensing capacity in different imaging applications. The CRA generates spatial codes in the imaging domain, which are dynamically changed through the excitation of multiple-input-multiple-output (MIMO) feeding arrays. In order to increase the sensing capacity of the CRA even further, frequency dispersive metamaterials can be designed to coat the surface of the CRA, which ultimately produces spectral codes in near- and far- fields of the reflector. This chapter describes different concepts of operation, in which a CRA can be used to perform active and passive sensing and imaging.

Keywords: compressive antenna, spatial and spectral coding, reflector antenna, metamaterial absorbers, sensing capacity

1. Introduction

Reducing the cost of electromagnetic (EM) sensing and imaging systems is a necessity before they can be far and widely established as a part of an extensive network of radars. Recently, a new beamforming technique based on a compressive reflector antenna (CRA) was proposed [1–6] to improve the sensing capacity of an active sensing system. This improvement has enhanced the information transfer efficiency from the sensing system to the imaging domain and vice versa. Thus, complexity and cost of the hardware architecture can be drastically

reduced. The beamforming that the CRA creates is based on multi-dimensional coding: (a) spatial coding by introducing dielectric or metallic scatterers on the surface of the reflector, (b) spectral coding by coating the reflector with metamaterials, and (c) temporal coding by the use of temporal multiplexing of transmitting and receiving horn arrays.

This unique feature of CRAs has triggered its use in a wide variety of applications, which include the following: (a) active imaging of metallic targets at mm-wave frequencies [1–3], (b) passive imaging of the physical temperature of the Earth at mm-wave frequencies [4, 5], and (c) active imaging of red blood cells at optical frequencies [6].

The proposed CRA beamforming technique, which may be used for imaging applications, is based on norm-1 regularized iterative Compressive Sensing (CS) algorithms. In this chapter, we also present the mathematical formulation that describes the properties of the spatial and temporal codes produced by the CRA that will be used to perform quasi real-time imaging.

The content outlined in this chapter leverages advances from multi-scale wave propagation, sparse data signal processing, information coding, and distributed computing. The result will enhance the efficiency and reliability of the current beamforming systems by using novel compressive sensors made of traditional metallic and dielectric structures, as well as novel metamaterials and meta-surfaces.

2. Compressive reflector antenna

The concept of operation of the CRA for sensing and imaging applications relies on two basic principles: (a) multi-dimensional coding, generated by the design of a customized reflector and (b) compressed sensing, performed on the under-sampled measured data.

The CRA is fabricated as described in Ref. [1]. **Figure 1** shows the cross-section of a traditional reflector antenna (TRA) ($x > 0$) and of a CRA ($x < 0$). The latter is built by introducing discrete scatterers, Ω_i, on the surface of the reflector, which are characterized by their size $\{D_i^x, D_i^y, D_i^z\}$ in $\{\hat{x}, \hat{y}, \hat{z}\}$, and by the electromagnetic constitutive properties $\{\sigma_i, \mu_i, \varepsilon_i\}$ (conductivity, permeability, and permittivity). These scatterers generate a pseudo-random time-space coded pattern in the near and far fields of the antenna after reflecting the incident field produced by the feeding elements. The temporal variation of these coded patterns allows the use of CS techniques to generate a 3D image of an object under test in the region of interest (ROI). The main difference between a CRA and a TRA is the use of the applique scatterers located on the surface of the former, as shown in **Table 1**.

2.1. Sensing matrix

There are many techniques that may be used to dynamically change these coded patterns, including but not limited to the following: (a) electronic beam steering by using a focal plane array or a reconfigurable sub-reflector, (b) electronic change of the constitutive parameters of the scatterers, and (c) mechanical rotation of the reflector along the $\hat{z}$-axis of the parabola.

http://dx.doi.org/10.5772/67663

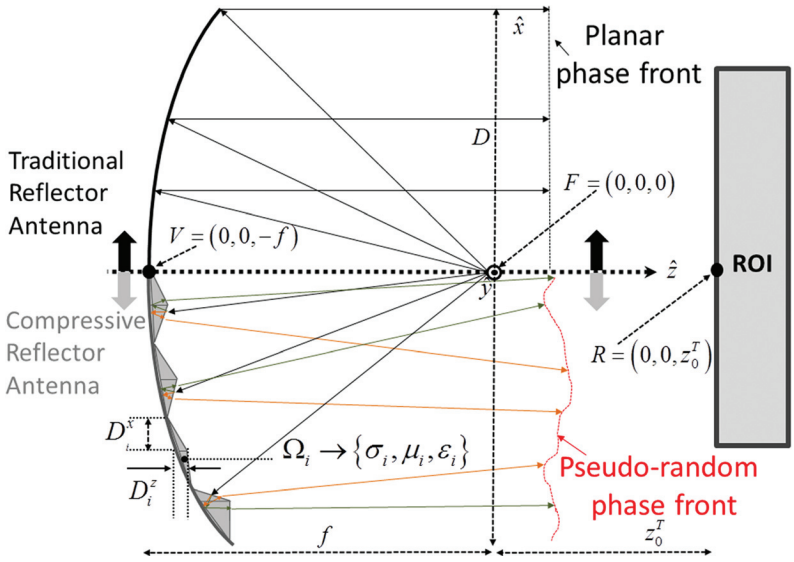

Figure 1. 2D cross-sections of a traditional reflector antenna ($x > 0$) and a compressive reflector antenna (CRA) ($x < 0$), where all the design parameters are described.

Parameter	TRA	CRA
D: aperture size	Same	
f: focal length	Same	
Ω_i: scatterer	No	Yes

Table 1. Comparison of the parameters of reflector antennas.

Let us focus on option 1, where an array of N_{Tx} transmitter and N_{Rx} receiver horns are arranged in a cross-shaped configuration around the focal point of the reflector, as shown in **Figure 2**. Each receiver collects the signal from each transmitter for N_f, different frequencies, for a total number of $N_m = N_{Tx} \cdot N_{Rx} \cdot N_f$ measurements. The image reconstruction is performed in N_p pixels, on an region of interest (ROI) located z_0^T meters away from the focal point of the CRA. Under this configuration, the sensing matrix $\mathbf{H} \in \mathbb{C}^{N_m \times N_p}$, computed as described in Ref. [7], establishes a linear relationship between the unknown complex reflectivity vector in each pixel, $\mathbf{u} \in \mathbb{C}^{N_p}$, and the measured complex field data $\mathbf{g} \in \mathbb{C}^{N_m}$. This relationship can be expressed in a matrix form, by applying the physical optics (PO) approximation to the total field and discretizing the integral operator as done in Ref. [8], as follows:

$$\mathbf{g} = \mathbf{H}\mathbf{u} + \mathbf{w}, \tag{1}$$

where $\mathbf{w} \in \mathbb{C}^{N_m}$ represents the noise collected by each receiving antenna, when the target is illuminated with a given transmitting antenna and for a given frequency.

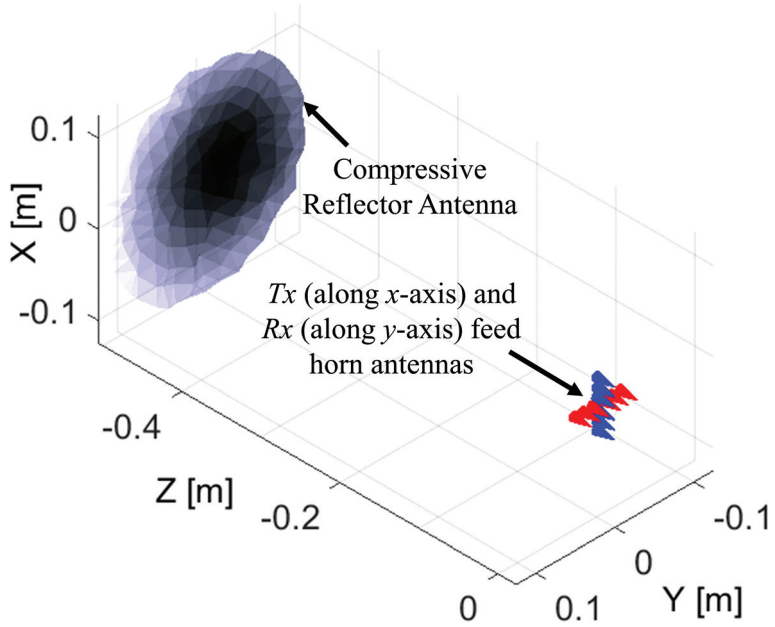

Figure 2. Geometry of the compressive reflector antenna with the feed horns at the focal plane.

Regardless of the configuration of the system, the sensing matrix will always have the dimensions $N_m \times N_p$, where N_m is the number of independent codes that are used—it depends on the configuration and the type of imaging system—and N_p is the total number of pixels in the imaging domain.

In order to impose sparsity on the solution of Eq. (1), a compressive sensing (CS) approach is used. CS theory was first introduced by Candes et al. [9], and it establishes that sparse signals can be recovered by the use of a reduced number of measurements when compared to those required by the Nyquist sampling criterion. In order to be able to apply such principles, the sensing matrix $\mathbf{H}$ must satisfy the Restricted Isometry Property (RIP) condition [10], which is related to the independence of its columns. Likewise, the number of nonzero values N_{nz} of the reconstructed image vector $\mathbf{u}$ must be much smaller than the total number of elements N_p (that is $N_{rz} \ll N_p$). Under the assumption that the two aforementioned conditions are satisfied, the reconstruction of the unknown vector $\mathbf{u}$ may be performed by solving the following optimization problem that only uses a reduced number of measurements $\mathbf{g}$:

$$\min \|\mathbf{u}\|_1 \quad \text{s.t.} \quad \|\mathbf{H}\mathbf{u} - \mathbf{g}\|_2 < \delta_H \tag{2}$$

where δ_H is an upper bound for the residual error $\|\mathbf{H}\mathbf{u} - \mathbf{g}\|_2$. Many algorithms for solving Eq. (2) have been developed [11, 12]. Here, a MATLAB toolbox NESTA [23] is used to solve that equation.

2.2. Sensing capacity of a compressive reflector antenna

The linearized sensing matrix **H** in Eq. (1) defines the properties of the imaging system, which can be interpreted as a multiple-input-multiple-output (MIMO) communications system [13]. The capability of the CRA to transmit information from the image domain **r** to the measured field domain **g**, in the presence of noise, can be studied by quantifying the capacity associated with the sensing matrix **H**. This sensing capacity of the imaging system can be derived from the singular value decomposition of **H**, as follows:

$$\mathbf{H} = \mathbf{U}\Sigma\mathbf{V}^{\star} \tag{3}$$

where $\mathbf{V} = (\mathbf{v_1}, \ldots, \mathbf{v}_{N_p})$ and $\mathbf{U} = (\mathbf{u_1}, \ldots, \mathbf{u}_{N_m})$ are, respectively, $N_p \times N_p$ and $N_m \times N_m$ matrices containing a set of orthonormal input- and output- based directions for **H**; the matrix $\Sigma = diag(\lambda_1, \ldots, \lambda_{N_{min}})$, where $N_{\min} = min(N_m, N_p)$, is an $N_p \times N_m$ matrix containing the real nonzero singular values of **H** in the diagonal and zeros elsewhere. When the *l–th* input base direction v_l is used in the image domain and propagated through the channel **H**, a $\lambda_l \mathbf{u}_l$ response is generated in the output-measured field domain. Therefore, $\{\lambda_l, \mathbf{v}_l, \mathbf{u}_l\}$ can be seen as the parameters of the *l–th* orthogonal channel of the matrix **H**. The $N_{\min}$ orthogonal parallel channels provide the following capacity, measured in bits [13]:

$$C = \sum_{l=1}^{N_{min}} \log_2\left(1 + \frac{P_l \lambda_l^2}{N_0}\right) \tag{4}$$

where P_l/N_0 is the signal to noise ratio (SNR) in the *l–th* orthogonal channel. The parameters $\{\sigma_i, \mu_i, \epsilon_i, D_i^x, D_i^y, D_i^z\}$ are used to modify and control the singular values of the matrix **H** and, therefore, to tailor the sensing capacity of the imaging system. One important feature that is often desired for a sensing and an imaging system is its ability to maximize the information transfer efficiency, that is, its sensing capacity, between the pixels in the region of interest and the sensors; this happens when the mutual information of successive measurements is reduced as much as possible. The pseudo-random spatial codes created by the CRA make successive measurements more independent, which ultimately results in measurements having reduced mutual information and providing enhanced imaging capabilities to the system.

2.3. Metamaterial absorber-based compressive reflector antenna

A metamaterial absorber (MMA) [4, 5, 13–15] , which was originally introduced by Landy et al. [15], poses a unique behavior that can be exploited for sensing and imaging applications. Specifically, by using an array of MMAs, in which each element of the array presents a near-unity absorption at a specified frequency, one can produce codes that are changed with the instantaneous frequency of the radar chirp, as presented in Ref. [16]. As a result, the number of transmitters and receivers required to achieve suitable imaging performance is drastically reduced. Coating the recently developed CRA with MMAs has the potential to further improve the antenna's imaging capabilities, in terms of sensing capacity (**Figure 3**) [1]. However, the utilization of the MMAs in doubly curved pseudo-randomly distorted compressive reflectors for imaging applications requires an accurate characterization of the bulk behavior of

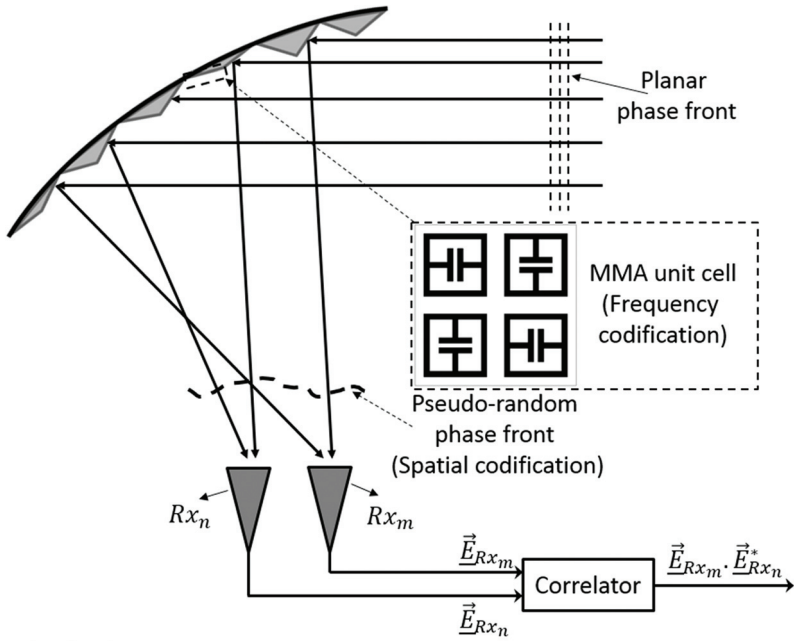

Figure 3. A 2D cross-section of an offset metamaterial-based CRA.

the metamaterial for dimensional scales involving several wavelengths and for oblique incidence on the MMAs. The MMA array can be characterized by solving a three-layer magneto-dielectric medium problem, where an incident field is obliquely impinging a magneto-dielectric medium of thickness d, which is backed by a metallic layer. The magneto-dielectric and metallic layers may be characterized by a Drude-Lorentz model [14]:

$$\tilde{\varepsilon}_r(\omega) = \varepsilon_{\text{inf}} + \frac{\omega_{p,e}^2}{\omega_{0,e}^2 - \omega^2 - i\gamma_e\omega}; \qquad \tilde{\mu}_r(\omega) = \mu_{\text{inf}} + \frac{\omega_{p,m}^2}{\omega_{0,m}^2 - \omega^2 - i\gamma_m\omega} \tag{5}$$

in which, ε_{inf} and μ_{inf} are the static permittivity and permeability at infinite frequency, $\omega_{p,e}$ and $\omega_{p,m}$ are the volume plasma frequencies at which the density of the electric and magnetic charges oscillate, $\omega_{0,e}$ and $\omega_{0,m}$ are the resonant frequencies, and γ_e and γ_m are the damping constants, which represent the electric and magnetic charge collision rate.

The reflection coefficient of this stratified three-layer magneto-dielectric medium can be analytically described as follows [17]:

$$\Gamma = \Gamma_{12} + \frac{T_{12}\Gamma_{23}T_{21}e^{-j2\Phi^{trans}}}{1 - \Gamma_{23}\Gamma_{21}e^{-2j\Phi^{trans}}} \tag{6}$$

where Γ is the total reflection coefficient of the structure, Γ_{ij} and T_{ij} are the reflection and transmission coefficients, associated with the interface between medium i and medium j, respectively, Φ^{trans} is the phase delay and the amplitude attenuation associated with the wave

traveling from the first interface into the second one, or vice versa, and $e^{-j\Phi^{trans}} = e^{-jk_2^t \cdot r} = e^{-j\beta_2^t \cdot r} \cdot e^{-\alpha_2^t \cdot r}$, with **r** being the distance vector and k_2^t being the complex wave vector. Although this model does not take anisotropy into consideration, it can be included in the model using the formulation described in Ref. [18].

2.4. Beamforming using compressive reflector antenna

When a TRA is illuminated from the focus (located at $z = 0$, without loss of generality, as **Figure 1** shows), a plane wave field is obtained in the focal aperture. The mathematical expression of this wave may be represented in terms of both spatial and time coordinates as follows:

$$g(x,y,z,t) = g_0(x,y,z)e^{j\omega_0 t}, \tag{7}$$

where $\omega_0 = 2\pi f_0$, with f_0 being the frequency of the wave. The spatial distribution of the field $g_0(x,y,z)$ can be split as $g_0(x,y,z) = A(z)I_\Omega(x,y)$, with $A(z)$ as the amplitude, which depends on the z position, and $I_\Omega(x,y)$ as an indicator function defined as follows:

$$I_\Omega(x,y) = \begin{cases} 1 & if \quad (x,y) \in \Omega \\ 0 & \text{otherwise,} \end{cases} \tag{8}$$

Ω being the domain of definition of the antenna, that is, the 2D projection of the reflector in the plane XY.

The radiation pattern in the far-field is related to the field in the aperture through a 2D Fourier transform as follows [19]:

$$\begin{aligned} G(\theta,\phi,z,t) = \mathbf{FT}[g(x,y,z,t)] &= \int_\Omega g_0(x,y,z)e^{j\omega_0 t}e^{jk_u x}e^{jk_v y}dxdy \\ &= A(z)e^{j\omega_0 t}\int_\Omega I_\Omega(x,y)e^{jk_u x}e^{jk_v y}dxdy = A(z)e^{j\omega_0 t}\mathbf{FT}[I_\Omega(x,y)], \end{aligned} \tag{9}$$

for $u = \sin(\theta)\cos(\phi)$ and $v = \sin(\theta)\sin(\phi)$.

In the case where applique scatterers are added to the surface of the reflector, so creating the compressive reflector antenna, the field in the focal aperture is not going to be uniform any more. It can be defined as follows:

$$\tilde{g}(x,y,z,f,t) = \tilde{g}_0(x,y,z,f)e^{j\omega_0 t}. \tag{10}$$

The new expression of the field depends as well on the frequency, and its spatial distribution can be expressed as follows:

$$\tilde{g}_0(x,y,z,f) = g_0(x,y,z)c(x,y,f). \tag{11}$$

The function $c(x,y,f)$ describes the changes on the focal aperture field with respect to that of a traditional reflector, due to the random rugosity in space and the random variation in frequency associated with the dispersive metamaterials. These functions are interpreted as codes.

The radiation pattern would now be determined, as well, in terms of the Fourier transform as follows [20]:

$$\tilde{G}(\theta,\phi,z,t,f) = \mathbf{FT}[\tilde{g}(x,y,z,t,f)] = \int_{\Omega} g_0(x,y,z)c(x,y,f)e^{j\omega_0 t}e^{jk_u x}e^{jk_v y}dxdy$$
$$= A(z)e^{j\omega_0 t}\int_{\Omega} I_{\Omega}(x,y)c(x,y,f)e^{jk_u x}e^{jk_v y}dxdy = \frac{1}{2\pi}A(z)e^{j\omega_0 t}\mathbf{FT}[I_{\Omega}(x,y)]**\mathbf{FT}[c(x,y,f)]. \quad (12)$$

In this way, the beamforming is performed by the 2D spatial convolution of the original pattern with the Fourier transform of the code. **Figure 4** shows the difference between the radiation pattern of a traditional reflector and that of a compressive reflector in one dimension.

In the general case, when an array of transmitters and receivers is arranged around the focal point of the reflector (**Figure 2**), the two-way radiation pattern for a traditional reflector is given by the product of the transmitting and receiving radiation patterns, $G_{Tx}(\theta,\phi,z,t)$ and $G_{Rx}(\theta,\phi,z,t)$, respectively [19]. These are defined by the Fourier transform of both the transmitter and receiver apertures, $g_{Tx}(x,y,z,t)$ and $g_{Rx}(x,y,z,t)$, respectively:

$$G_{TR}(\theta,\phi,z,t) = G_{Tx}(\theta,\phi,z,t)G_{Rx}(\theta,\phi,z,t)$$
$$= \mathbf{FT}[g_{Tx}(x,y,z,t)]\mathbf{FT}[g_{Rx}(x,y,z,t)] = \mathbf{FT}[g_{Tx}(x,y,z,t)**g_{Rx}(x,y,z,t)]. \quad (13)$$

In the case of the compressive reflector antenna, the two-way radiation pattern will be determined by the product of the transmitting and receiving radiation patterns, $\tilde{G}_{Tx}(\theta,\phi,z,t,f)$ and $\tilde{G}_{Rx}(\theta,\phi,z,t,f)$, respectively, considering, as well, the codes in space and frequency:

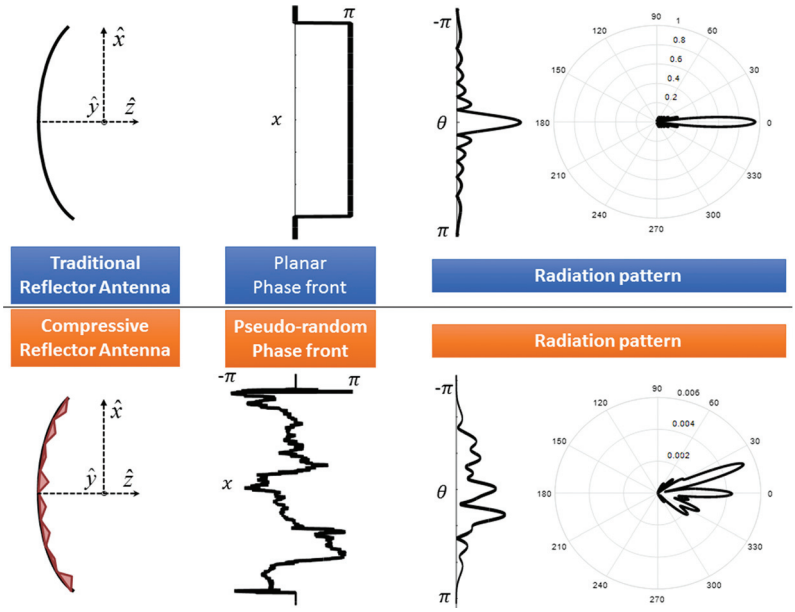

Figure 4. Top: A 2D cross-section of a traditional reflector antenna, planar phase front distribution, and a radiation pattern with a main lobe. Bottom: A 2D cross-section of a compressive reflector antenna, pseudo-random phase front distribution, and a radiation pattern with multiple lobes.

http://dx.doi.org/10.5772/67663

$$\begin{aligned}\tilde{G}_{TR}(\theta,\phi,z,t,f) &= \tilde{G}_{Tx}(\theta,\phi,z,t,f)\tilde{G}_{Rx}(\theta,\phi,z,t,f)\\ &= \mathbf{FT}[\tilde{g}_{Tx}(x,y,z,t,f)]\mathbf{FT}[\tilde{g}_{Rx}(x,y,z,t,f)] = \mathbf{FT}[\tilde{g}_{Tx}(x,y,z,t,f)**\tilde{g}_{Rx}(x,y,z,t,f)]\\ &= \mathbf{FT}[g_{Tx}(x,y,z,t)c_{Tx}(x,y,f)**g_{Rx}(x,y,z,t)c_{Rx}(x,y,f)]\\ &= \frac{1}{4\pi^2}\Big(\mathbf{FT}[g_{Tx}(x,y,z,t)]**\mathbf{FT}[c_{Tx}(x,y,f)]\Big)\Big(\mathbf{FT}[g_{Rx}(x,y,z,t)]**\mathbf{FT}[c_{Rx}(x,y,f)]\Big)\\ &= \frac{1}{4\pi^2}\Big(G_{Tx}(\theta,\phi,z,t)**C_{Tx}(\theta,\phi,f)\Big)\Big(G_{Rx}(\theta,\phi,z,t)**C_{Rx}(\theta,\phi,f)\Big),\end{aligned} \tag{14}$$

where $C_{Tx/Rx}(\theta,\phi,f) = \mathbf{FT}[c_{Tx/Rx}(x,y,f)]$. That is, the radiation pattern of transmitting and receiving arrays is convolved with the 2D spatial Fourier transform of the transmitting and receiving codes, respectively, and then multiplied. In this way, the beamforming is performed. Examples of radiation patterns for different CRA configurations are shown in **Figure 5**. The abovementioned formulations are combined with the method of moments in order to compute the scattered fields. The simulation results for a $15\lambda \times 15\lambda \times 2\lambda$ metallic, dielectric, and metamaterial bulk scatterers are presented in **Figure 5**. These simulations show the feasibility of using the CRA in order to generate wide pseudo-random sub-beam-like codes. These codes are produced not only in the near-field region but also in the far-field region of the CRA.

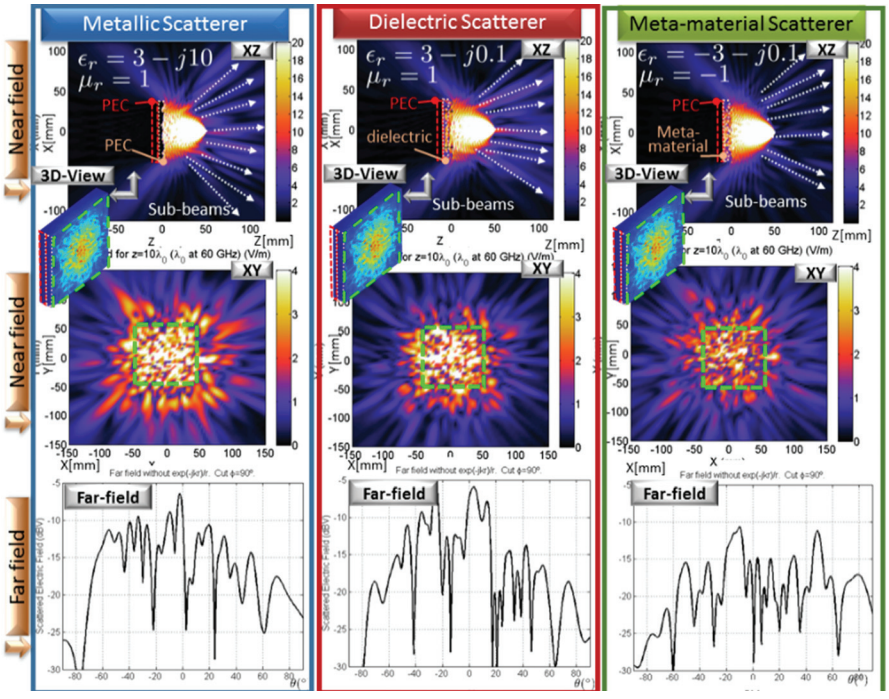

Figure 5. Multi-lobe radiation pattern representation for different scatterer configurations of a CRA.

The aforementioned electronic beamforming technique has been analyzed using a focal plane array on the proposed CRA. Point Spread Function (PSF) of the array is studied to measure the focusing efficiency of the system. The PSF can be evaluated by applying a phase compensation method. Specifically, the phase produced by each transmitting and receiving code of the CRA in the imaging region is adjusted in order to produce a zero phase at any desired focusing point. As a result, a constructive interference is obtained after adding all the codes that are in-phase at the focusing point, and a destructive interference is obtained elsewhere. The phased array consists of 12 equidistant transmitters on a vertical line on the focal plane, while the receiver elements are located similarly in a horizontal line. Eighteen frequencies are used in the range of 70–77 GHz to perform the beamforming, and the reflector has a diameter of 35 cm and a focal distance of 35 cm. **Figures 6** and **7** show the

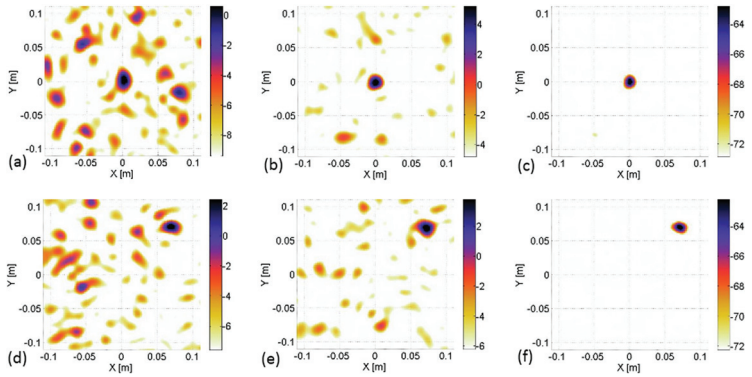

Figure 6. (a) PSF of the CRA with PEC scatterers. The focusing point is at [0, 0, 84] cm for (a), (b), and (c) and at [7, 7, 84] cm for (d), (e), and (f). (a) and (d) are the E-field patterns of the transmitters, (b) and (e) are the E-field patterns of the receivers, and (c) and (f) are the product of the E-field patterns of the transmitters and receivers.

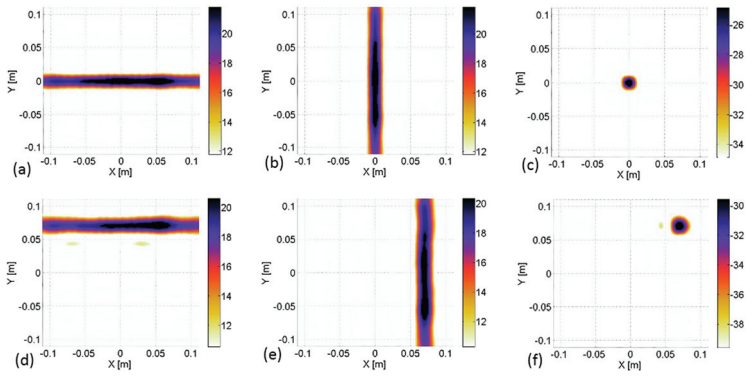

Figure 7. PSF of the CRA with MMAs. The focusing point is at [0, 0, 84] cm for (a), (b), and (c) and at [7, 7, 84] cm for (d), (e), and (f). (a) and (d) are the E-field patterns of the transmitters, (b) and (e) are the E-field patterns of the receivers, and (c) and (f) are the product of the E-field patterns of the transmitters and receivers.

simulated PSF of the CRA with perfect electric conductor (PEC) scatterers and MMAs, respectively. The triangle size of the PEC scatterers is 5λ, and MMAs are used to produce 16 different codes in the frequency domain. The imaging plane is located 84 cm far from the focal point.

3. Applications

In this section, the performance of the CRA for active and passive imaging applications is studied and compared to that of conventional systems. In all examples, the sensing capacity and image reconstruction of the systems are presented. It has been shown that the sensing capacity of the CRA is improved when compared to that of conventional imaging systems, and, as a result, a better image reconstruction can be achieved.

3.1. Active imaging

The performance of the CRA is evaluated in an active imaging application [1]. For this experiment, we use a mechanical rotation of the reflector along the $\hat{z}$-axis of the parabola, from 0 to θ_r degrees in N_θ steps.

Each scatterer Ω_i of the CRA is made of a PEC $(\sigma_i = \sigma_{PEC})$. The CRA is discretized into triangular patches, as described in Ref. [7], that are characterized by an average size of $< D^x >=< D^y >$ in $\hat{x}$ and $\hat{y}$ dimensions. The parameter λ_c is the wavelength at the center frequency. The scatterer size D_i^z of each triangle in $\hat{z}$ is modeled as a uniform random variable. The ROI is located at z_0^T away from the focal point of the CRA, and it encloses a volume determined by the following dimensions: Δx_0^T in $\hat{x}$, Δy_0^T in $\hat{y}$, and Δz_0^T in $\hat{z}$. The ROI is discretized into cubes of side length l. The total number of measurements (rows in **H**) is $N_m = N_\theta \cdot N_f$, and the total number of pixels for the imaging reconstruction (columns in **H**) is N_p. The parameters described in **Table 2** are used for the numerical simulation.

Three different configurations are analyzed in this example: (a) a TRA without scatterers on its surface, (b) a CRA with a feeding horn located in the focal point of the reflector (CRA-in-focus), and (c) a CRA with a feeding horn displaced $\Delta R^X = 10\lambda_c\hat{x} = 0.05\hat{x}\ m$ off the focal point of the reflector (CRA-off-focus). **Figure 8** shows the structure of the CRA, and **Figure 9** depicts the spatial codes generated by the CRA-off-focus antenna for five different rotation angles in a 2D plane of the ROI.

Figure 10(a) shows the singular values for the three configurations. The TRA presents only three singular values greater than -50 dB, and, as a result, its capacity is reduced when compared to that provided by any of the CRA configurations. Rotation of the CRA antenna makes the off-focus configuration illuminate different sections of the reflector, thus producing different spatial codes in the region of interest; the CRA-in-focus illuminates the same spatial region of the CRA when it is rotated around its axis. This methodology makes the CRA-off-focus have a singular value distribution with less dispersion than the CRA-in-focus, which

Parameters	Value	Parameters	Value
Center frequency (f_c)	$60GHz$	No. of measurements (N_m)	93
Wavelength at center frequency (λ_c)	$5mm$	No. of pixels in ROI (N_p)	25000
Bandwidth	$6GHz$	$< D^x >=< D^y >$	$1.5\lambda_c$
Reflector diameter (D)	$100\lambda_c = 0.5m$	D_i^z	$U(\mp 0.54\lambda_c)$
Focal length (f)	$100\lambda_c = 0.5m$	z_0^T	$194.87\lambda_c$
Maximum rotation (θ_r)	90^0	$\Delta x_0^T = \Delta y_0^T$	$36\lambda_c$
No. of rotations (N_θ)	31	Δz_0^T	$7.5\lambda_c$
No. of frequencies (N_f)	3	Length size of cubes l	$1.5\lambda_c$

Table 2. Parameters of the numerical design.

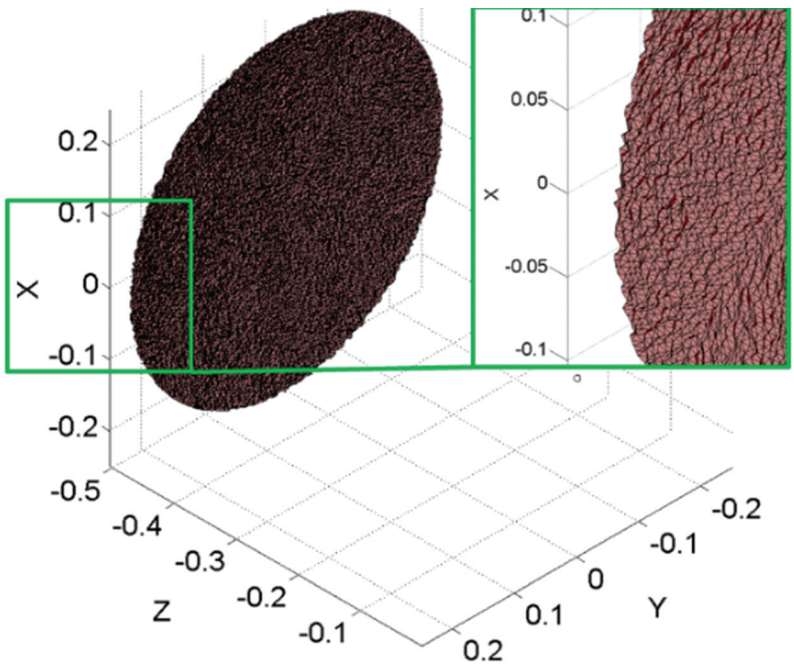

Figure 8. A 3D view of the CRA (left), and an augmented view of the pseudo-random scatterers (right).

ultimately provides the highest capacity of the three configurations in Eq. (4). **Figure 10(b)** shows the sensing capacity of the three configurations for different signal to noise ratios, and it can be seen that the CRA-off-focus clearly outperforms the other two configurations.

http://dx.doi.org/10.5772/67663

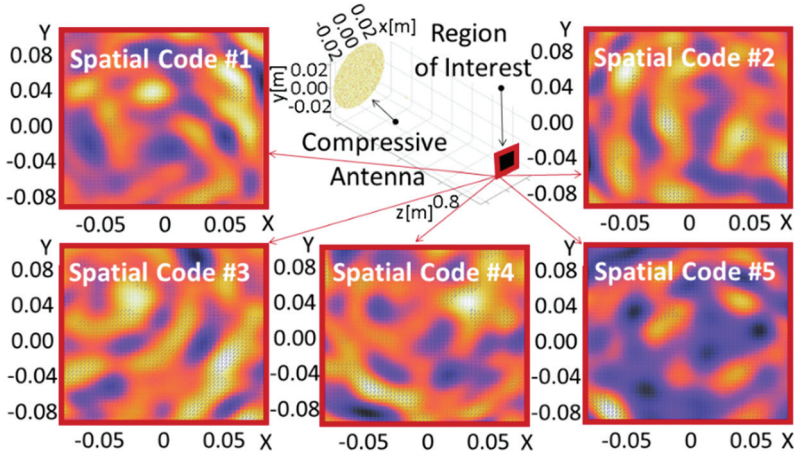

Figure 9. CRA and spatial codes generated in a 2D plane of the ROI for five rotation angles.

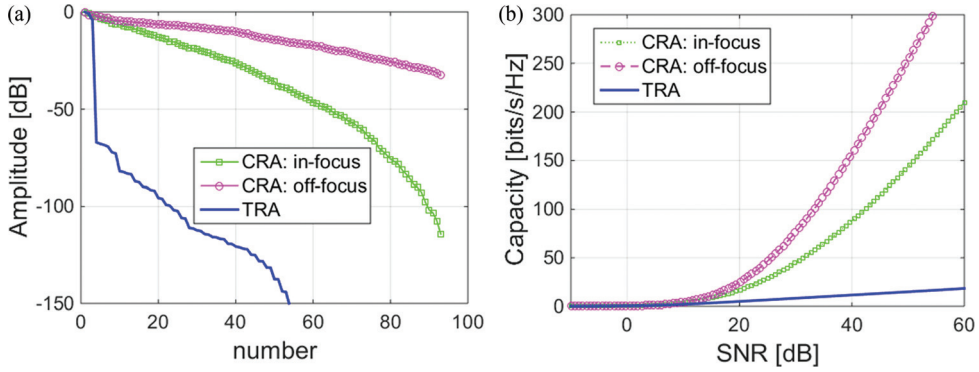

Figure 10. (a) Singular values in a logarithmic scale for the three configurations and (b) capacity as a function of the signal to noise ratio for the three configurations.

Figure 11 shows the imaging results. A uniform white noise producing a signal to noise ratio of 25 dB is used in the simulation. The target is represented by the transparent triangles with the black border. **Figure 11(a)** shows that, albeit CS is used, the sensing capacity of the in-focus CRA is not enough, and it fails to recover all the targets in the scene. However, the proposed off-focus CRA configuration is able to reconstruct objects with a sparsity level similar to that shown in **Figure 11(b)**. Notwithstanding, increasing the number of targets in the ROI may require additional measurements, which may be obtained from data collected at additional frequencies and/or rotation angles. The additional data results in an increment on the number of rows in the sensing matrix.

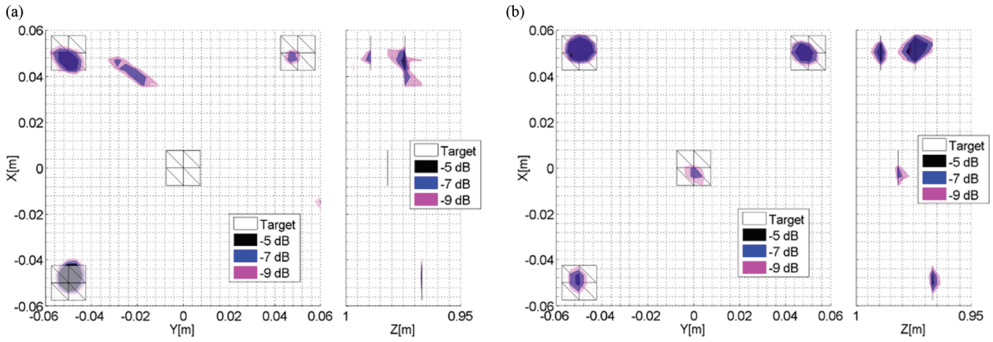

Figure 11. A front and a side view of the reconstructed normalized reflectivity function of the high sensing capacity using CS for (a) in-focus and (b) off-focus CRAs.

3.2. Array of CRAs for active imaging

In this example, the imaging system is composed of six CRAs positioned in a cross-shaped configuration, as shown in **Figure 12(a)**, each with an array of transmitters and receivers. The design parameters for each one of the reflectors are shown in **Table 3**. Both the vertical receiving array and the horizontal transmitting array of each CRA consist of 18 uniformly distributed conical horn antennas as shown in **Figure 12(b)**. The radar operates in the 70–77 GHz frequency band, and 10 frequencies are used to perform the imaging.

Each CRA is designed to effectively be able to image over a projected circular area of 40 cm diameter in the cross range region (see solid-line circles in **Figure 12(a)**) when the target is located 90 cm away from the focal plane. It is important to note that additional shaping

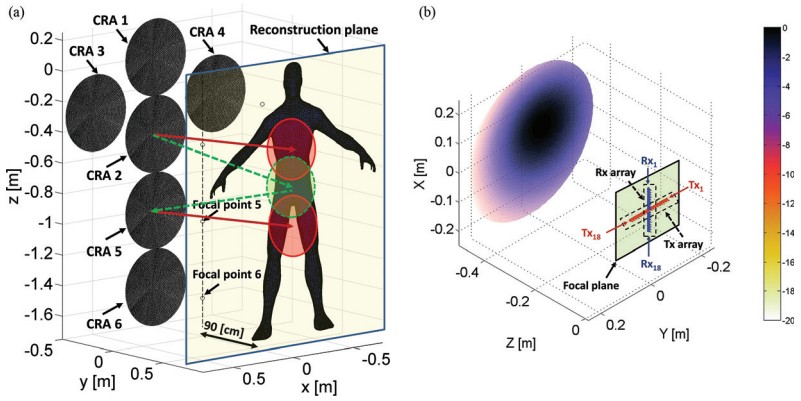

Figure 12. (a) A 3D view of the proposed millimeter-wave sensing system composed of six CRAs and (b) induced currents on a CRA excited by Tx1. The feeding transmitter (along *y*-axis) and receiver (along *x*-axis) arrays are located on the focal plane of the reflector.

Parameters	Value	Parameters	Value
Frequency band	70–77 GHz	No. of Tx	18
No. of frequencies (N_f)	10	No of Rx	18
Reflector diameter (D)	50 cm	$\langle D^x \rangle = \langle D^y \rangle$	2 cm
Focal length (f)	50 cm	D_i^z	Uniform (−10.5, +10.5) mm
Range (z_0^T)	90 cm		

Table 3. Design parameters for a single CRA.

techniques could have been used to image over a wider projected cross range region. The CRA has an aperture size of 50 cm, and, as a result, none of the two adjacent CRAs will be able to image the region located between their two circular projections (see the dashed-line circle in **Figure 12(a)**). This drawback can be easily solved by coupling the information coming from the adjacent reflectors in a multi-static fashion, as illustrated by the two dashed-line arrows in **Figure 12(a)**. Given the aforementioned location of the target, this work only considered the electromagnetic cross-coupling between CRA-l and CRA-k, where l and k take the following values: (l = 1, k = 2), (l = 1, k = 3), (l = 1, k = 4), (l= 2, k = 5), and (l = 5, k = 6).

The performance of the proposed active system is evaluated in a mm-wave imaging application, using a PO method [7]. The target used in the simulation is a tessellated model of a human body. In this work, the 3D human model was projected into a 2D plane, located 90 cm away from the focal plane, and its extension to 3D will be a future line of investigation. **Figure 13(a)** shows the improved singular value distribution of a single CRA when compared to that of a TRA, and **Figure 13(b)** shows how the sensing capacity of the CRA is enhanced for different SNRs.

Finally, **Figure 14** demonstrates that the proposed imaging system is capable of accurately reconstructing the target under investigation (note that the hands are out of the region of interest).

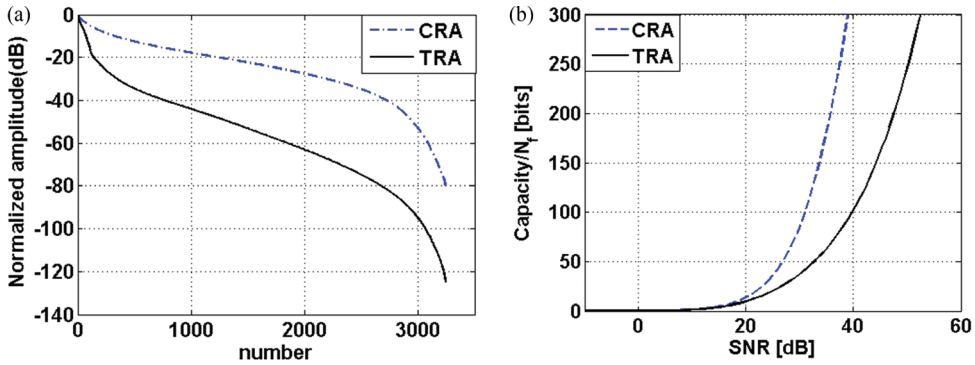

Figure 13. Comparison of (a) the normalized singular value distribution and (b) the sensing capacity of a single CRA and TRA.

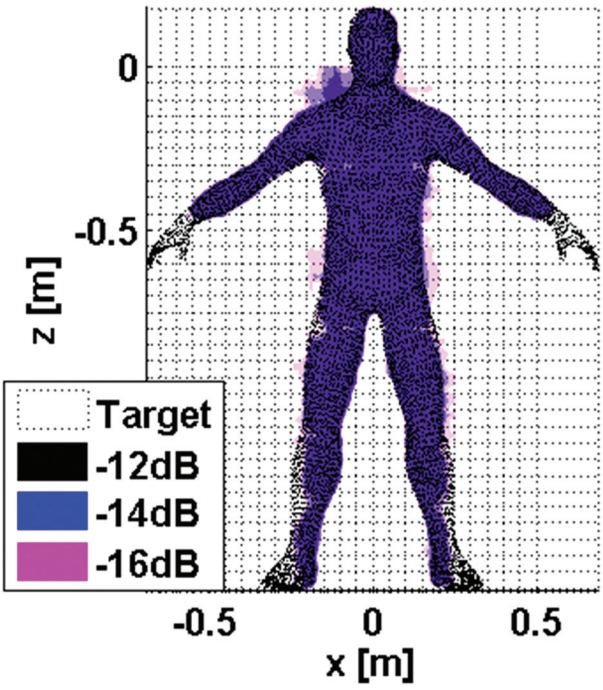

Figure 14. A reconstructed image using an iterative compressive sensing algorithm (NESTA).

3.3. Passive imaging

Using the mechanism introduced in Section 2.3, by describing the magneto-dielectric medium with the Drude-Lorentz model, three MMA types (MMA1, MMA2, and MMA3), resonating at three different frequencies (50 GHz, 52 GHz, and 54 GHz), are designed and randomly coated on the surface of the PEC scatterers, as shown in **Figure 15**. The polarization-independent electric-field-coupled absorber (ELCA) is designed using the commercially available software high-frequency structural simulator (HFSS)—a finite element-based full-wave solver [21]. Built-in master/slave boundary conditions in HFSS were utilized to simulate the planar MMA unit cell with periodic boundary conditions. Next, the Drude-Lorentz parameters of the three-layer magneto-dielectric medium are optimized to match the reflection coefficient of the model and the one obtained from HFSS for a given incident angle. The pattern search method embedded in the MATLAB optimization toolbox was used to solve the optimization problem. The optimized Drude-Lorentz parameters for MMA2 resonating at 52 GHz are as follows: $\varepsilon_{\text{inf}} = 2.9$, $\omega_{p,e} = 2\pi \times 9.01\,GHz$, $\omega_{0,e} = 2\pi \times 52\,GHz$, $\gamma_e = 2\pi \times 341\,MHz$, $\mu_{\text{inf}} = 3.1$, $\omega_{p,m} = 2\pi \times 7.55\,GHz$, $\omega_{0,m} = 2\pi \times 52\,GHz$, and $\gamma_m = 2\pi \times 291\,MHz$.

The performance of the designed metamaterial-based CRA interferometric system is evaluated in a microwave sounding imaging application, and it is then compared to that of a conventional interferometric system (GeoSTAR). The GeoSTAR system [22] is an interferometer, and its operation is based on performing complex cross-correlations between the measured fields by

http://dx.doi.org/10.5772/67663

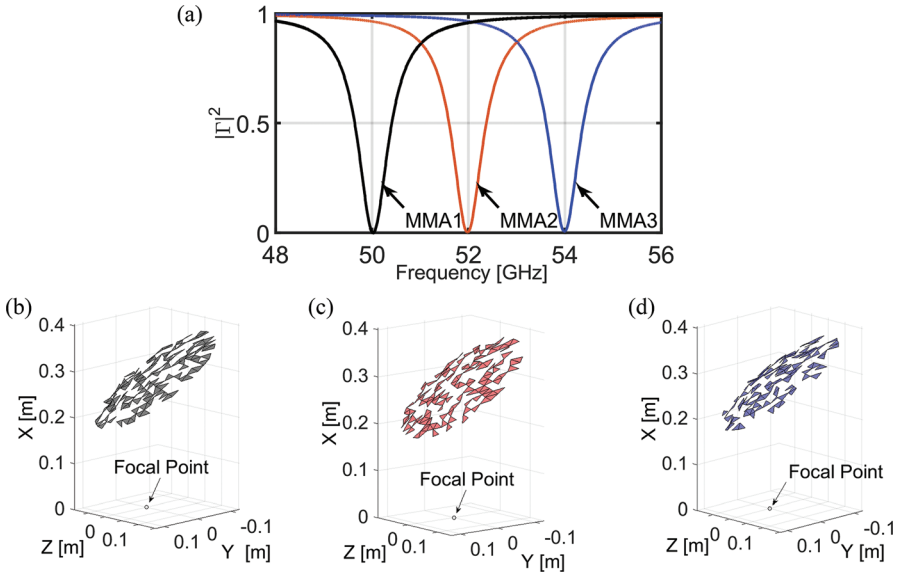

Figure 15. (a) Magnitude of the reflection coefficient and PEC scatterer facets associated with (b) MMA1, (c) MMA2, and (d) MMA3.

each pair of receivers in a Y-shaped array. These complex cross-correlated signals, which are characterized by the spatial coherence function of the electromagnetic field, are used to reconstruct the physical temperature of the Earth's atmosphere. For solving the inverse problem, a traditional pseudo-inverse method and a current state-of-the-art compressive sensing algorithm (NESTA) [23] are used.

The design parameters used for the numerical simulation are shown in **Table 4**. Nine receiving horns, which are placed in a Y-shaped configuration on the focal plane, are used to feed the metamaterial-based CRA. **Figure 16** shows a comparison of the geometry of the metamaterial-based CRA and GeoSTAR systems. The original image (**Figure 17(a)**) is an example of the physical temperature radiated from the surface of the Earth, and the system is assumed to measure EM fields from a geostationary satellite orbiting around the Earth. To ensure a fair

Parameters	CRA configuration	GeoSTAR configuration
Frequency band	50–54 GHz	50–54 GHz
Number of frequencies (N_f)	7	7
Longest Aperture size (D)	25 cm	25 cm
Diameter of feed elements	2.1 cm	2.1 cm
Number of feeds (N_r)	9	18
Focal length (f)	14 cm	–
Offset height (h_o)	28 cm	–

Table 4. Parameters for the numerical design.

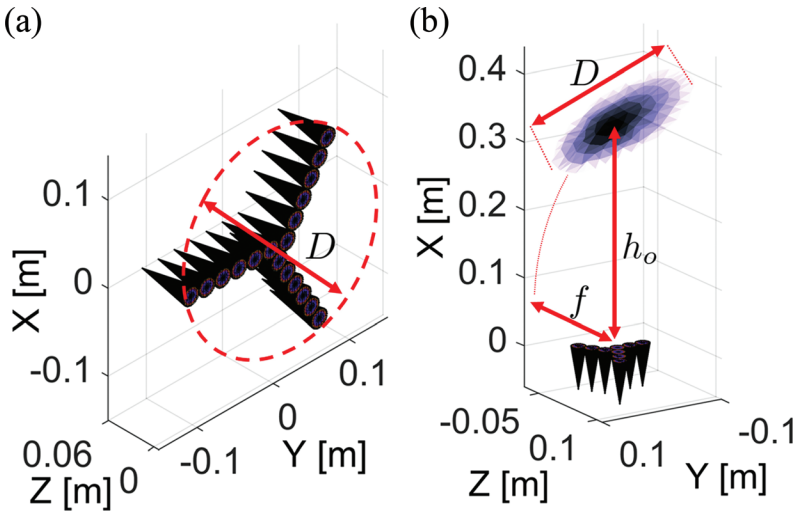

Figure 16. Geometry: (a) GeoSTAR configuration and (b) compressive reflector antenna.

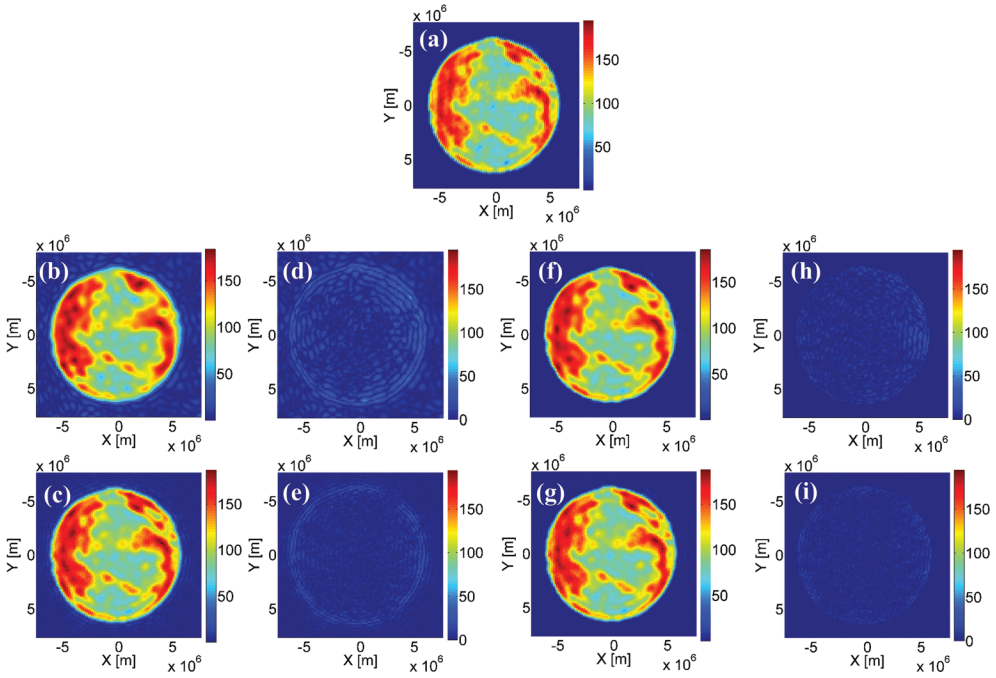

Figure 17. Image reconstruction for the metamaterial-based CRA and GeoSTAR configurations: (a) Original image; reconstruction with pseudo-inverse method for (b) metamaterial-based CRA, and (c) GeoSTAR; error in pseudo-inverse method for (d) metamaterial-based CRA, and (e) GeoSTAR; reconstruction with iterative NESTA method for (f) metamaterial-based CRA, and (g) GeoSTAR; error in NESTA method for (h) metamaterial-based CRA, and (i) GeoSTAR.

analogy between our system and the GeoSTAR system, the frequency range and the largest dimension of the aperture for both configurations are set to be equal. However, the metamaterial-based CRA uses only one-half of the horns required by the GeoSTAR configuration, resulting in less data required for the reconstruction.

Figure 17 shows the original and reconstructed images for the metamaterial-based CRA and GeoSTAR configurations. The error is computed using the Frobenius norm of the difference between the original and the reconstructed images, and it is normalized by the Frobenius norm of the original image. The reconstructed physical temperature using the pseudo-inverse method for the metamaterial-based CRA and the GeoSTAR configuration produces an error of 16.7 and 8.6%, respectively.

The error value of the CS NESTA imaging algorithm for the metamaterial-based CRA and the GeoSTAR configuration is 6.9 and 5.5%, respectively. This shows that the number of receivers are substantially reduced for the metamaterial-based CRA when compared to that of a GeoSTAR system (from 18 to 9), while keeping similar imaging performance.

4. Conclusion

In this chapter, a novel beamforming technique based on CRA for sensing and imaging applications was presented. The CRA uses PEC scatterers and/or MMAs on the surface of the reflector to generate spatial and spectral electromagnetic codes in the imaging domain. The CRA has the ability to increase the sensing capacity of the imaging system, which maximizes the information transfer efficiency. The CRA can reduce the number of feeding elements; therefore, it results in a reduction of the energy budget and the system's complexity. Different examples for active and passive imaging in the mm-wave band were discussed in this chapter. In all examples, the sensing capacity of the CRA was improved when compared to that of the TRA, which ultimately results in a better image reconstruction.

Acknowledgements

This work has been partially funded by the National Science Foundation, CAREER program, Award No. 1653671, and by the Department of Homeland Security, Award No. 2013-ST-061-ED0001. The authors would like to thank Dr. Hipolito Gomez Sousa and Prof. Oscar Rubinos Lopez, from University of Vigo, for their collaboration in the generation of **Figure 5**.

Author details

Ali Molaei[1], Juan Heredia Juesas[1,2] and Jose Angel Martinez Lorenzo[1,2]*

*Address all correspondence to: jmartinez@coe.neu.edu

1 Electrical & Computer Engineering, Northeastern University, Boston, Massachusetts, USA

2 Mechanical & Industrial Engineering, Northeastern University, Boston, Massachusetts, USA

References

[1] Martinez-Lorenzo JA, Heredia-Juesas J, Blackwell W. A single-transceiver compressive reflector antenna for high-sensing-capacity imaging. IEEE Antennas and Wireless Propagation Letters. 2016;**15**:968–971.

[2] Heredia-Juesas J, Blackwell W. Single-transceiver compressive antenna for high-capacity sensing and imaging applications. In: 9th European Conference on Antennas and Propagation (EuCAP); 2015, pp. 1–3.

[3] Heredia-Juesas J, Allan G, Molaei A, Tirado L, Blackwell W, Lorenzo. Consensus-based imaging using ADMM for a compressive reflector. In: IEEE International Symposium on Antennas and Propagation & USNC/URSI National Radio Science Meeting; 2015, pp. 1304–1305.

[4] Molaei A, Heredia-Juesas J, Allan G, Martinez-Lorenzo J. Active imaging using a metamaterial-based compressive reflector antenna. In: IEEE International Symposium on Antennas and Propagation (APSURSI), IEEE; 2016, pp. 1933–1934.

[5] Molaei A, Allan G, Heredia-Juesas J, Blackwell W, Martinez-Lorenzo J. Interferometric sounding using a compressive reflector antenna. In: 10th European Conference on Antennas and Propagation (EuCAP), IEEE; 2016, pp. 1–4.

[6] Gomez-Sousa H, Rubinos-Lopez O, Martinez-Lorenzo JA. Hematologic characterization and 3d imaging of red blood cells using a compressive nano-antenna and ml-fma modelling. In: Antennas and Propagation (EUCAP2016); 2016.

[7] Meana JG, Martinez-Lorenzo JA, Las-Heras F, Rappaport C. Wave scattering by dielectric and lossy materials using the modified equivalent current approximation (MECA). IEEE Transactions on Antennas and Propagation, 2010;**58**(11):3757–3761.

[8] Martinez-Lorenzo JA, Quivira F, Rappaport C. SAR imaging of suicide bombers wearing concealed explosive threats. Progress in Electromagnetics Research. 2012;**125**:255–272.

[9] Candes EJ, Romberg JK, Tao T. Stable signal recovery from incomplete and inaccurate measurements. Communication on Pure and Applied Mathematics, 2006;**59**(8):1207–1223.

[10] Rish I, Grabarnik G. Sparse modeling: theory, algorithms, and Applications. Boca Raton, FL: CRC Press; 2014.

[11] Massa A, Rocca P, Oliveri G. Compressive sensing in electromagnetics—a review. IEEE Antennas and Propagation Magazine, 2015;**57**(1):224–238.

[12] Oliveri G, Anselmi N, Massa A. Compressive sensing imaging of non-sparse 2d scatterers by a total-variation approach within the born approximation. IEEE Transactions on Antennas and Propagation, 2014;**62**(10):5157–5170.

[13] Tse D, Viswanath P. Fundamentals of wireless communication. Cambridge University Press; 2005.

[14] Watts CM, Liu X, Padilla WJ. Metamaterial electromagnetic wave absorbers. Advanced Materials, 2012;**24**(23):98–120.

[15] Landy NI, Sajuyigbe S, Mock JJ, Smith DR, Padilla WJ. Perfect metamaterial absorber. Physical Review Letters, 2008;**100**(20):207402.

[16] Hunt J, Driscoll T, Mrozack A, Lipworth G, Reynolds M, Brady D, Smith DR. Metamaterial apertures for computational imaging. Science. 2013;**339**(6117):310–313.

[17] Chew WC. Waves and fields in inhomogeneous media. New York: IEEE Press; 1995, 522 p.

[18] Ding W, Chen L, Liang CH. Characteristics of electromagnetic wave propagation in biaxial anisotropic left-handed materials. Progress in Electromagnetics Research, 2007; **70**:37–52.

[19] Ahmed SS, Schiess A, Schmidt LP. Near field mm-wave imaging with multistatic sparse 2D-arrays. In: European Radar Conference (EuRAD); 2009.

[20] Bracewell R. The Fourier transform and its applications. McGraw-Hill; 1965.

[21] Ansys HF. v15. Pittsburgh, PA: ANSYS Corporation Software; 2014.

[22] Lambrigtsen B, Tanner A, Gaier T, Kangaslahti P, Brown S. Prototyping GeoSTAR for the PATH mission. In: Proceedings NASA Science Technology Conference; 2007, pp. 19–21.

[23] Nesterov Y. Smooth minimization of non-smooth functions. Mathematical Programming, 2005;**103**(1):127–152.